The Astronomical Journal, 167:217 (15pp), 2024 May https://doi.org/10.3847/1538-3881/ad306b

Elemental Abundances in the Diffuse Interstellar Medium from Joint Far-ultraviolet and X-Ray Spectroscopy: Iron, Oxygen, Carbon, and Sulfur

I. Psaradaki[1,2,3], L. Corrales[2], J. Werk[4], A. G. Jensen[5], E. Costantini[3], M. Mehdipour[6], R. Cilley[2], N. Schulz[1], J. Kaastra[3], J. A. García[7,8], L. Valencic[9], T. Kallman[7], and F. Paerels[10]
[1] MIT Kavli Institute for Astrophysics and Space Research, 70 Vassar Street, Cambridge, MA 02139, USA
[2] LSA, University of Michigan, 1085 South University Avenue, Ann Arbor, MI 48109, USA
[3] SRON Netherlands Institute for Space Research, Niels Bohrweg 4, 2333 CA Leiden, The Netherlands
[4] University of Washington, Seattle, WA 98195, USA
[5] University of Nebraska at Kearney, Department of Physics and Astronomy, 2502 19th Avenue, Kearney, NE 68849, USA
[6] Space Telescope Science Institute, 3700 San Martin Drive, Baltimore, MD 21218, USA
[7] X-ray Astrophysics Laboratory, NASA Goddard Space Flight Center, Greenbelt, MD 20771, USA
[8] Cahill Center for Astrophysics, California Institute of Technology, Pasadena, CA 91125, USA
[9] Johns Hopkins University, 3400 North Charles Street, Baltimore, MD 21218, USA
[10] Columbia Astrophysics Laboratory and Department of Astronomy, Columbia University, 550 West 120th Street, New York, NY 10027, USA
Received 2023 December 22; revised 2024 March 3; accepted 2024 March 4; published 2024 April 15

Abstract

In this study, we investigate interstellar absorption lines along the line of sight toward the galactic low-mass X-ray binary Cygnus X-2. We combine absorption line data obtained from high-resolution X-ray spectra collected with the Chandra and XMM-Newton satellites, along with far-UV absorption lines observed by the Hubble Space Telescope's (HST) Cosmic Origins Spectrograph (COS) instrument. Our primary objective is to understand the abundance and depletion of oxygen, iron, sulfur, and carbon. To achieve this, we have developed an analysis pipeline that simultaneously fits both the UV and X-ray data sets. This novel approach takes into account the line-spread function of HST/COS, enhancing the precision of our results. We examine the absorption lines of Fe II, S II, C II, and C I present in the far-UV spectrum of Cygnus X-2, revealing the presence of at least two distinct absorbers characterized by different velocities. Additionally, we employ `Cloudy` simulations to compare our findings concerning the ionic ratios for the studied elements. We find that gaseous iron and sulfur exist in their singly ionized forms, Fe II and S II, respectively, while the abundances of C II and C I do not agree with the Cloudy simulations of the neutral ISM. Finally, we explore discrepancies in the X-ray atomic data of iron and discuss their impact on the overall abundance and depletion of iron.

Unified Astronomy Thesaurus concepts: Chemical abundances (224)

1. Introduction

The interstellar medium (ISM) is an important component of our Galaxy—it contributes to many astrophysical processes and the formation of new stars. The ISM evolves dynamically and is divided into different phases. The *neutral phase* contains atomic gas at temperatures from $\sim 10^2$ to $\sim 10^{3.7}$ K, and *molecular gas* can be found either in gravitationally bound clouds or in the diffuse ISM. These are typically cool regions ($\sim$10 K), and their density can vary from $\sim$1000 cm^{-3} up to $\sim 10^6$ cm^{-3}. Finally, the *ionized phase* describes the ISM regions with temperatures from $\sim 10^4$ up to $\sim 10^{5.5}$ K, which is called the warm ionized medium or hot ionized medium respectively (e.g., Tielens 2001; Draine 2011). A multiwavelength approach provides the means to better understand the structure of the ISM. UV absorption spectroscopic observations can probe gas-phase abundances through resonance transitions, while X-rays can also provide spectroscopic information about the solid phase. In this work, we use the combination of UV and X-ray spectra to better determine the elemental abundances in the ISM.

1.1. Oxygen

Oxygen is the most abundant cosmic element after H and He, and the amount depleted into dust grains is highly variable with ISM phase. The overall estimate of the oxygen budget in the ISM remains highly uncertain, as noted by Jenkins (2009). Although it is anticipated that oxygen may experience some depletion into dust, a considerable portion of it appears to be absent from the gaseous phase, without a comprehensive explanation. The combined contribution of carbon monoxide (CO), ices, silicate, and oxide dust particles is insufficient to fully account for the missing oxygen in the denser regions of the ISM, particularly at the interface where the diffuse and dense ISM meet, as highlighted by Whittet (2010) and Poteet et al. (2015). Oxygen has been extensively studied in the literature using high-resolution X-ray spectroscopy of the O K-edge (Takei et al. 2002; Juett et al. 2004; de Vries & Costantini 2009; Pinto et al. 2010, 2013; Costantini et al. 2012; Gatuzz et al. 2014, 2016; Joachimi et al. 2016; Eckersall et al. 2017). In Psaradaki et al. (2020, 2023), we studied the oxygen abundance in both gas and solids through the O K-edge. We found that about 10%–20% of the neutral oxygen is depleted into dust, and that in the diffuse sight lines, the oxygen abundance is consistent with or slightly above the solar value. In this work, we examine the X-ray and UV features simultaneously.

1.2. Iron

Iron is a major constituent in most dust grain models, as more than 90% of the total iron is depleted from the gas phase; the remainder is presumably locked up in dust grains

(e.g., Savage & Bohlin 1979; Jenkins et al. 1986; Snow et al. 2002; Jenkins 2009). More than 65% of the iron is injected into the ISM in gaseous form by Type Ia supernovae; therefore, most of the Fe dust growth is expected to take place in the ISM (Dwek 2016). However, the exact composition of Fe-bearing grains as well as the exact amount and form that iron takes in the ISM is still unclear. Iron is expected to be present in silicate dust grains, but it could also exist in pure metallic nanoparticles (e.g., Kemper et al. 2002) or even as metallic inclusions in glass with embedded metal and sulfides (GEMS), suspected to be of interstellar origin (e.g., Bradley 1994; Altobeli et al. 2016; Ishii et al. 2018). The possibility of iron sulfides is discussed in more detail below.

UV and optical observations find that the remaining gas-phase Fe is primarily in the form of Fe II in neutral regions of the ISM (Snow et al. 2002; Jensen & Snow 2007; Miller et al. 2007). This is because the ionization potential of Fe I is 7.87 eV, and it can be ionized by photons coming from the interstellar radiation field (ISRF) with energies between 7.87 eV and the Lyman limit at 13.6 eV. The ionization potential of Fe II is 16.18 eV, which lies above the cutoff energy of the ISRF and is thereby unlikely to get ionized. In H II regions, the gas-phase iron should be a mix of Fe II, Fe III, and Fe IV. In H II regions, some Fe I may exist, but due to depletion rates as high as 99% found in cold neutral regions (e.g., Savage & Sembach 1996), it is more likely to be in dust grains.

1.3. Sulfur

The degree to which interstellar sulfur is depleted is still a matter of debate (Jenkins 2009). In the diffuse ISM, sulfur is expected to have modest depletion (Costantini et al. 2019 and references therein). However, in denser regions, such as molecular clouds, sulfur can be included in aggregates such as H_2S and SO_2 (Duley et al. 1980). Sulfur in dust has been detected near C-rich asymptotic giant branch stars, planetary nebulae (Hony et al. 2002), and protoplanetary disks (Keller & Messenger 2013). Solid Fe–S compounds are abundant in planetary system bodies, such as interplanetary dust particles, meteorites, and comets (e.g., Wooden 2008). The presence of sulfur in dust grains can also be associated with GEMS (Bradley 1994), where the FeS particles are concentrated on the surface of the glassy silicate. Metallic Fe particles embedded in a silicate matrix have become a popular model for explaining the depletion patterns of the ISM (e.g., Zhukovska et al. 2018). The Stardust mission revealed sulfur in the form of FeS, suspected to be of ISM origin (Westphal et al. 2014). This evidence revitalizes the idea that sulfur could be present in dust species, as well as in less dense ISM environments (Costantini et al. 2019). However, it has been shown that GEMS are a less-favored candidate of interstellar dust (Keller & Messenger 2011, 2013; Westphal et al. 2019).

In recent X-ray studies of interstellar Fe absorption, appreciable quantities of iron sulfide material like troilite (FeS), pyrite Peru (FeS_2), and ferrous sulfate ($FeSO_4$) are not found (Psaradaki et al. 2023; Corrales et al. 2024, submitted). Moreover, Gatuzz et al. (2024) carried out a recent X-ray study of the sulfur K-edge. The authors estimated column densities of ionic species of sulfur along with column densities of dust compounds for a sample of 36 low-mass X-ray binaries. Upper limits were obtained for most sources including the dust components. However, they found that the cold–warm column densities tend to decrease with the Galactic latitude, with no correlation with distance or Galactic longitude. S I has an ionization potential of 10.36 eV, below the Lyman limit, so the majority of gas-phase S in the neutral medium is expected to be in the form of S II. This work examines S II gas through the far-UV (FUV) triplet transition at 1250.6, 1253.8, and 1259.5 Å.

1.4. Carbon

Carbon is also suspected to be a major constituent of interstellar dust grains; however, we have limited knowledge about the amount of carbon that is locked up in dust grains (Jenkins 2009). It has been suggested that carbon constitutes around 20% of the total depleted mass in the Galaxy (Whittet 2003; Draine & Hensley 2021). Its depletion covers a relatively narrow range of values, showing that it is not a strong function of environmental density (Costantini et al. 2019). The majority of carbon should be locked in graphite grains, providing a likely explanation for the 2175 Å emission feature (Draine 1989, 2003, and references therein). However, concerns have been raised regarding the insufficiency of carbon depletion to account for the observed optical properties of interstellar dust (Kim & Martin 1996; Dwek 1997; Mathis 1998). A broad interstellar absorption feature at 2175 Å as well as narrow-band emission features in the far-IR are attributed to polycyclic aromatic hydrocarbons (e.g., Draine 1989, 2003). Various carbonaceous grain compositions proposed include graphite, hydrogenated amorphous carbon, and silicates with carbonaceous mantles (Duley et al. 1989; Weingartner & Draine 2001; Zubko et al. 2004; Jones et al. 2017; Costantini et al. 2019). Carbon could also be locked in nanodiamonds, which could be created from graphite and amorphous carbon grains in high-pressure ISM environments, for example, around shocks (Tielens et al. 1987). Nanodiamonds are also found in meteoritic material, and isotopic ratios imply that they are not from the solar system. However, our knowledge of the actual depletion of carbon—and thereby the total amount of carbonaceous interstellar dust—is still an enigma.

Carbon spectroscopy of Galactic sources is usually challenging in the X-ray due to very high absorption as well as the relative insensitivity of modern X-ray instruments near the C K photoelectric absorption edge at 0.3 keV. However, it is possible for very low column density sight lines. Gatuzz et al. (2018) studied the C K-edge using high-resolution Chandra spectra of four novae during their super-soft-source phase. The authors detected resonances of C II Kα as well as the C III Kα and Kβ transitions. Moreover, simultaneous examination of the X-ray and UV spectrum of the extragalactic source Mrk 509 (Pinto et al. 2012) suggests that most of the neutral carbon is locked up in dust, while the bulk of C II comes from the warm photoionized phase. In this work, we study gas-phase carbon in the FUV through the C I and C II transition at 1328.8 and 1335.7 Å, respectively.

We use the joined information from X-ray data through the Chandra and XMM-Newton satellites and FUV data from the Cosmic Origins Spectrograph (COS) on board the Hubble Space Telescope (HST) in order to understand the abundance and depletion of oxygen, iron, sulfur, and carbon. In the last decades, high-resolution X-ray absorption spectroscopy has proven to be a powerful tool for studying the ISM (e.g., Wilms et al. 2000; Takei et al. 2002; Juett et al. 2004; Ueda et al. 2005; Pinto et al. 2010; García et al. 2011; Costantini et al. 2012; Pinto et al. 2013; Gatuzz et al. 2016; Joachimi et al. 2016; Schulz et al. 2016;

Table 1
Observation Log

Satellite	ObsID	Instrument/Mode	Exposure Time (ks)
HST	lb2m02010	COS/FUV/G130M	7
	lb2m03010	COS/FUV/G130M	7
	lb2m04010	COS/FUV/G130M	7
XMM-Newton	0303280101	RGS	32
	0561180501	RGS	24
Chandra	8170	HETGS/CC	65
	8599	HETGS/CC	60

Note. CC is an acronym for continuous clocking mode.

Yang et al. 2022). In particular, in the X-ray, we are able to study the solid-phase composition of highly depleted elements, such as iron in the line of sight toward a bright background source.

X-ray absorption fine structures are spectroscopic features observed near the photoelectric absorption edges of solid material (dust), and their shape is the ultimate footprint of the chemical composition, size, and crystallinity (e.g., Newville 2014; Lee & Ravel 2005; Corrales et al. 2016; Zeegers et al. 2017; Rogantini et al. 2018, 2019; Corrales et al. 2019; Zeegers et al. 2019; Psaradaki et al. 2020; Costantini & Corrales 2022; Psaradaki et al. 2023). However, the abundance and absorption strength of Fe II, likely the largest repository of gas-phase iron, is difficult to constrain from the X-ray band alone (Psaradaki et al. 2023; Corrales et al. 2024, submitted). In this pilot study, we use the joint information of the FUV and X-ray absorption spectra of the low-mass X-ray binary Cygnus X-2 to study both the gas and dust components of the ISM, providing the most comprehensive means possible to determine the abundances and depletion of prevalent interstellar elements. Cygnus X-2 is a bright X-ray source with a moderate column density ($2 \times 10^{21}\,\mathrm{cm}^{-2}$) and high flux ($2.3 \times 10^{-9}\,\mathrm{erg\,s}^{-1}\,\mathrm{cm}^{-2}$ in the 0.3–2 keV band), making it an excellent target to study the diffuse ISM in the O K- and Fe L-edges. This sight line also exhibits a rich FUV spectrum with absorption signatures from the ISM. The distance of the source has been estimated to be around 7–12 kpc (Cowley et al. 1979; McClintock et al. 1984; Smale 1998; Yao et al. 2009). This paper is organized as follows. In Section 2, we present the HST/COS, Chandra, and XMM-Newton data used in this study and their reduction processes. In Section 3, we describe the adopted method for analyzing the FUV spectra, and in Sections 4 and 5, we discuss the spectral fitting to the X-ray data. Finally, in Section 6, we discuss the results, and we give our conclusions in Section 7.

2. Data Reduction

The HST/COS data sets for Cygnus X-2, described in Table 1, were downloaded from the MAST Portal archive.[11] All the data sets were obtained using the G130M filter. They consist of separate files for each of the two FUV detector segments, segment A and segment B. We reduce and combine the data sets for both segments using the documented instructions in the HST user page.[12]

We further obtained the Cygnus X-2 data sets from the XMM-Newton Reflection Grating Spectrometer (RGS; den Herder et al. 2001), which has a resolving power of $R = \frac{\lambda}{\Delta\lambda} \gtrsim 400$ and an effective area of approximately 45 cm^2 in the spectral region of interest. The data sets were downloaded from the XMM-Newton archive[13] (Table 1) and reduced using standard calibration procedures of the Science Analysis Software (SAS; v.18). We created the event lists by running the *rgsproc* command. Then, we filtered the RGS event lists for flaring particle background using the default value of 0.2 counts s^{-1} threshold. We excluded the bad pixels using `keepcool=no` in the SAS task *rgsproc*. Moreover, when the spectral shape does not vary through different epochs and the spectra can be superimposed, we combined the data using the SAS command rgscombine. This allowed us to obtain a single spectrum with a higher signal-to-noise ratio.

The Chandra observations used in this work were downloaded from the Transmission Grating Catalogue[14] (Huenemoerder et al. 2011). Chandra carries two high-spectral-resolution instruments, the High Energy Transmission Grating (HETGS; Canizares et al. 2005) and the Low Energy Transmission Grating (Brinkman et al. 2000). The HETGS consists of two sets of gratings, the Medium Energy Grating (MEG) and the High Energy Grating. In this study, we are mainly interested in Fe L-shell photoelectric absorption edges. We therefore used HETGS/MEG due to its high throughput and spectral resolution ($R = \frac{\lambda}{\Delta\lambda} \gtrsim 660$) around the Fe L-edges. For each observation, we combine the positive and negative orders of dispersion using the X-ray data analysis software, CIAO (version 4.11; Fruscione et al. 2006). The persistent emission of the source is steady, and we therefore combine the different observations using the CIAO tool `combine_grating_spectra`.

3. The FUV Spectrum

The HST/COS instrument covers a wavelength range of the FUV absorption lines that is useful for this study. In particular, we examine the COS spectrum of Cygnus X-2 in the range of 1132–1280 and 1288–1430 Å for segments B and A, respectively. We studied in detail the absorption features of Fe II (1142.36 and 1143.22 Å), S II (1250.6 and 1253.8 Å), C I (1328.7 Å), C II (1335.7 Å), and O I (1302.16 Å).

We use the spectral models of pySPEX,[15] the python version of the software SPEctral X-ray and UV modeling and analysis, `SPEX` (Kaastra et al. 2018; version 3.06.01). Even though `SPEX` is primarily used for X-ray spectral analysis, its ability to model UV spectra with X-rays simultaneously has been demonstrated in the past (e.g., Pinto et al. 2013). We modified the `SPEX` atomic databases to ensure that the rest-frame wavelengths and oscillator strengths for the ions of interest come from the same study (Morton 1991). In Table 2, we present the wavelength and oscillator strength of each individual line used in this study. In the case of strong transitions and saturated lines, the derived column density was based on full Voigt profile fitting of the line features, which includes the damping wings. The exact value of the rest-frame velocity of each individual ion studied here, together with its

[11] https://mast.stsci.edu/portal/Mashup/Clients/Mast/Portal.html
[12] https://hst-docs.stsci.edu/cosdhb/chapter-5-cos-data-analysis/5-1-data-reduction-and-analysis-applications
[13] http://nxsa.esac.esa.int/nxsa-web/
[14] http://tgcat.mit.edu/tgSearch.php?t=N
[15] https://spex-xray.github.io/spex-help/pyspex.html

Table 2
Oscillator Strength (f_{ij}) and Rest-frame Wavelength (λ) Used in This Study Based on Morton (1991)

Ion	λ (Å)	f_{ij}
Fe II	1142.36	$5.00 \cdot 10^{-3}$
	1143.22	$1.33 \cdot 10^{-2}$
S II	1250.58	$5.45 \cdot 10^{-3}$
	1253.81	$1.08 \cdot 10^{-2}$
C I	1328.83	$5.804 \cdot 10^{-2}$
C II	1335.7	$1.15 \cdot 10^{-1}$
O I	1302.16	$4.88 \cdot 10^{-2}$

oscillator strength, will be important for the calculation of the ionic column densities.

SPEX allows us to measure the column density of individual absorption lines using the slab model. This model calculates the absorption by a slab of optically thin gas, where the column densities of ions are fitted individually and are independent of each other. The free parameters are the ionic column density (N_i in cm^{-2}, where i is the ion), the Doppler shift (z_v in $km\,s^{-1}$), and the rms broadening of the observed absorption line (b in $km\,s^{-1}$). SPEX is designed to work with X-ray calibration files, which are differently designed than those used to analyze UV data. Consequently, we developed a Python procedure that uses SPEX to determine a physical model for the FUV data set and then convolves that model with the COS line-spread function (LSF) for the wavelength of interest following the HST/COS users' manual.[16] The LSF describes the light distribution at the focal plane as a function of wavelength in response to a monochromatic light source. The dominant effect in the observed spectrum is a broadening of the spectral features and the filling in of saturated line features due to the finite resolution of the instrument. COS LSFs are known to have non-Gaussian wings, and a model of the LSF is needed to perform accurate line profile fitting.

We used the Markov Chain Monte Carlo (MCMC) analysis package *emcee* (Foreman-Mackey et al. 2013) for the final spectral fitting. The *emcee* package employs an ensemble sampler to probe the model parameter space. It uses the Metropolis–Hastings algorithm, which enables sampling from multidimensional distributions. We used the χ^2 statistic (Pearson 1900) to characterize the model likelihood for the UV data sets. We did not use priors, and for the burn-in phase, we initiated the walkers using normal distributions around the initial values provided by an initial fit in SPEX with a 25% dispersion. We ran *emcee* with 180 walkers and 65 steps for the burn-in phase, then ran the MCMC sampler for 260 steps to arrive at a posterior probability distribution. In the spectra obtained from HST/COS, we can observe distinct velocity components for all the lines under investigation (Figure 1). These lines reveal the presence of two absorbing clouds, each characterized by different velocity properties. Specifically, the absorption lines originating from the Fe II ion exhibit the presence of two blueshifted components: one with a velocity shift of $-37 \pm 4\,km\,s^{-1}$ and another with $-96 \pm 5\,km\,s^{-1}$. Similarly, the S II lines display two distinct components, one situated at $-20 \pm 2\,km\,s^{-1}$ and the other at $-84 \pm 2\,km\,s^{-1}$ relative to the rest-frame velocity. Furthermore, both S II and C II lines appear to be slightly saturated.

Our first fitting procedure solved for the ionic column density of the two absorptions components (N_i), the line-of-sight velocity shift (z_v), and their velocity broadening (b). Due to the fact that column density can be degenerate with the velocity broadening, we performed a second fit with the velocity broadening b frozen to the best-fitting value found in the first *emcee* run. This provides a stronger constraint on the ionic column densities. The best-fit parameters for all ions with their 1σ intervals are listed in Table 3. The best fits to all FUV lines are presented in Figure 1. An example of the MCMC posterior distribution is presented in Figure 2 for the S II lines. The illustrated corner plot shows the posterior distribution with two-dimensional histograms comparing each pair of free parameters including the velocity broadening, b. In the Figure 2 inset, we present the posterior distribution for the same number of iterations and walkers, but this time b is fixed to the fitted values. When the b parameter is fixed, the posterior distribution exhibits a symmetrical distribution, whereas when the parameter is left free, we observe a degeneracy between the velocity broadening and the ionic column density.

4. The X-Ray Spectrum: Fe L-edges

The high-resolution X-ray spectrum of Cygnus X-2 includes the narrow absorption lines produced by neutral and ionized gas in the ISM around the photoabsorption edges of Ne K (13.5 Å), O K (23 Å), and Fe L (17.5 Å). In this part of the study, we are interested in the spectral region that contains the Fe L-edges, so we limit our fitting to the narrow range of 15–19 Å. For this study, we combine the capabilities of both the Chandra and XMM-Newton satellites.

We use the available plasma models in SPEX in order to fit the HETGS/MEG and RGS spectra of Cygnus X-2 jointly. We bin the data by a factor of 2, which improves the signal-to-noise while the data are still oversampling the spectral resolution of the instruments and we are not losing accuracy. We adopt C-statistics (C_{stat}) to evaluate the goodness of fit (Cash 1979; Kaastra 2017). The models adopt the protosolar abundance units of Lodders & Palme (2009). To take into account the continuum variability among the different data sets, we use the sectors option in SPEX. Each data set can be allocated to a different sector, which allows us to fit the continuum parameters for each data set independently. As we are fitting a relatively narrow energy band, the full shape of the spectral energy distribution cannot be constrained. Thus, we fit the continuum using a phenomenological power law (pow model in SPEX) and a blackbody component (bb). The free parameters consist of the slope and normalization of the pow component and the temperature and normalization of the bb.

To take into account neutral Galactic absorption, we adopt the hot model of SPEX (de Plaa et al. 2004; Steenbrugge et al. 2005). For a given temperature and set of abundances, this model calculates the ionization balance and then determines all the ionic column densities scaled to the prescribed total hydrogen column density. At low temperatures ($\sim$0.001 eV $\sim$ 10 K), the hot model mimics a neutral gas in collisional ionization equilibrium, and the free parameters are the hydrogen column density in the line of sight and the temperature (kT, where k is the Boltzmann constant). In the diffuse ISM, the gaseous-phase iron is expected to be

[16] https://www.stsci.edu/hst/instrumentation/cos/performance/spectral-resolution

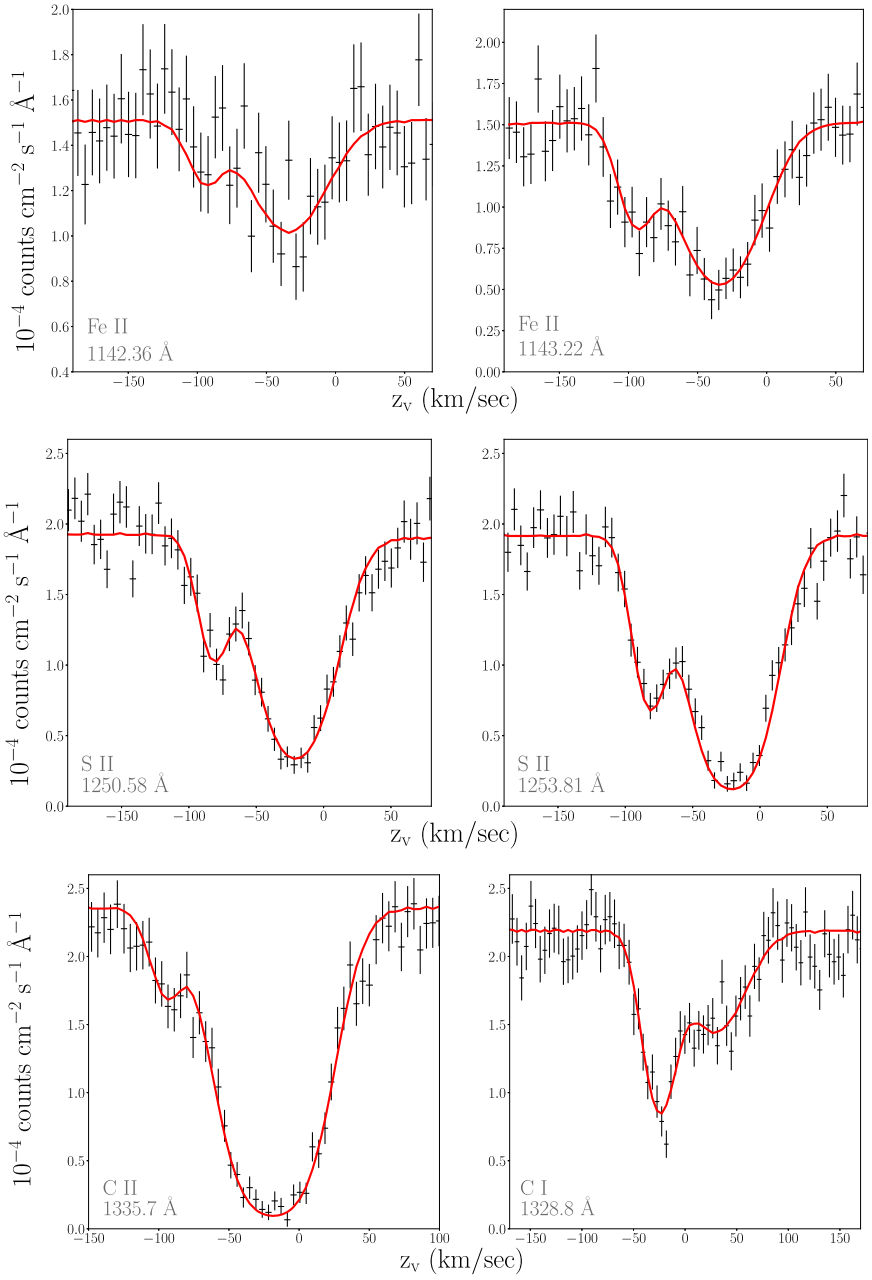

Figure 1. COS/FUV absorption lines and best-fit model for Fe II, S II, C I, and C II in velocity space.

Table 3
Best-fit Parameters for All the Observed Ions and Velocity Components Using SPEX and *emcee*

Ion	N_i (10^{15} cm^{-2})	z_v (km s^{-1})	b (km s^{-1})
Fe II	1.7 ± 0.3	-37 ± 4	25 ± 2
	0.3 ± 0.2	-96 ± 5	10 ± 1
S II	$7.4^{+1.3}_{-0.8}$	-20 ± 2	18 ± 2
	$1.9^{+8}_{-0.7}$	-84 ± 2	5 ± 3
C I	$0.21^{+0.09}_{-0.05}$	-25 ± 3	8^{+5}_{-1}
	$0.15^{+0.06}_{-0.04}$	26^{+10}_{-12}	30^{+12}_{-15}
C II	0.47 ± 0.03	-19 ± 2	26 ± 2
	<0.04	-95 (frozen)	<21

predominantly in the form of Fe II (e.g., Snow et al. 2002; Jensen & Snow 2007) due to ionization by the ISRF. To model Fe II, we set the Fe abundance of the `hot` neutral gas model to 0 and replace it with the `slab` model in SPEX. The abundance of Fe II is frozen to the value found from the fit of the HST/COS spectrum, shown in Table 3.

Around 90%–99% of interstellar Fe is known to be depleted into dust (e.g., Dwek 2016; Psaradaki et al. 2023). We use the `amol` model in SPEX, which calculates the transmission of a dust component, and leave the dust column density as a free parameter. We use the recently implemented dust extinction cross sections for the Fe L-edges (Psaradaki 2021; E. Costantini et al. 2024, in preparation), computed from laboratory data and presented in Psaradaki et al. (2020, 2023)

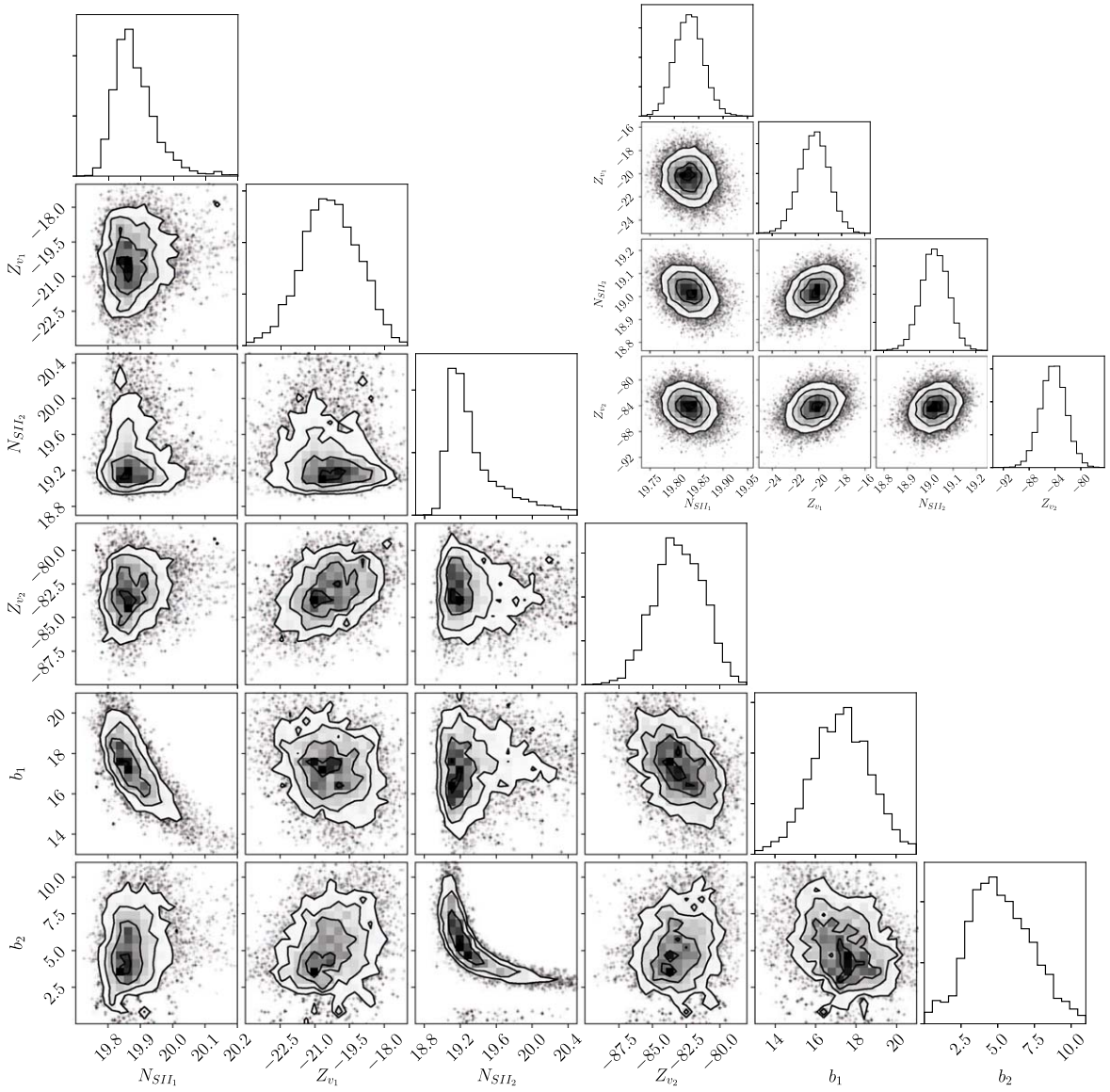

Figure 2. The posterior distribution for S II is plotted with two-dimensional histograms comparing each pair of free parameters. The contours represent the confidence levels of 1σ, 2σ, etc. $N_{\rm S\ II}$ is the logarithmic ionic column density in cm^{-2}, z_v is the velocity shift of each component in km s^{-1}, and b is the velocity broadening in km s^{-1}. The inset displays the identical posterior distribution, where the velocity-broadening parameter is fixed to the fitted value.

and Psaradaki (2021). The dust models have been computed using anomalous diffraction theory (van de Hulst 1957) and assuming a Mathis–Rumpl–Nordsieck (MRN) dust size distribution (Mathis et al. 1977). MRN follows a power-law distribution, $dn/da \propto a^{-3.5}$, where a is the grain size with a minimum cutoff of 0.005 μm and a maximum cutoff of 0.25 μm. Psaradaki et al. (2023) found that amorphous pyroxene ($Mg_{0.75}Fe_{0.25}SiO_3$) on average accounts for 80% of the dust mass, with metallic iron taking up the remaining 20%. This result on the silicate mixture of dust is broadly consistent with studies in infrared wavelengths (Min et al. 2007) and dust depletion studies (Konstantopoulou et al. 2024). In this context, it is important to clarify that we employ the term "amorphous" as a collective term for all noncrystalline materials. As explained in Psaradaki et al. (2020), our amorphous samples exhibit a glassy nature, with their structure potentially retaining a short-range order of atoms. Nevertheless, the Si K-edge spectra of these amorphous samples exhibit a distinctively smooth profile, contrasting significantly with crystal samples (Zeegers et al. 2019). We start by fitting the X-ray spectrum of Cygnus X-2 assuming this type of dust mineralogy.

The free parameters of our fit are the column density for each dust component and the parameters of the continuum model including $N_{\rm H}$. The depletion of silicon and magnesium is fixed to be at least 90% according to literature values (Rogantini et al. 2019; Zeegers et al. 2019), and the depletion of oxygen is constrained to be at least 20% (Psaradaki et al. 2023). The best fit is shown in Figure 3, with $C_{\rm stat}/{\rm dof} = 1098/736$. As discussed in Psaradaki et al. (2023), the remaining residuals around 17.6 Å are possibly due to the MRN grain size distribution assumed in this study (E. Costantini et al. 2024, in preparation). MRN provides a typical grain size distribution, while a larger grain size is able to produce a larger scattering component of the extinction cross section (e.g., Corrales et al. 2016; Zeegers et al. 2017). Dust size distributions larger than the MRN (larger maximum cutoff) will be examined in a follow-up paper.

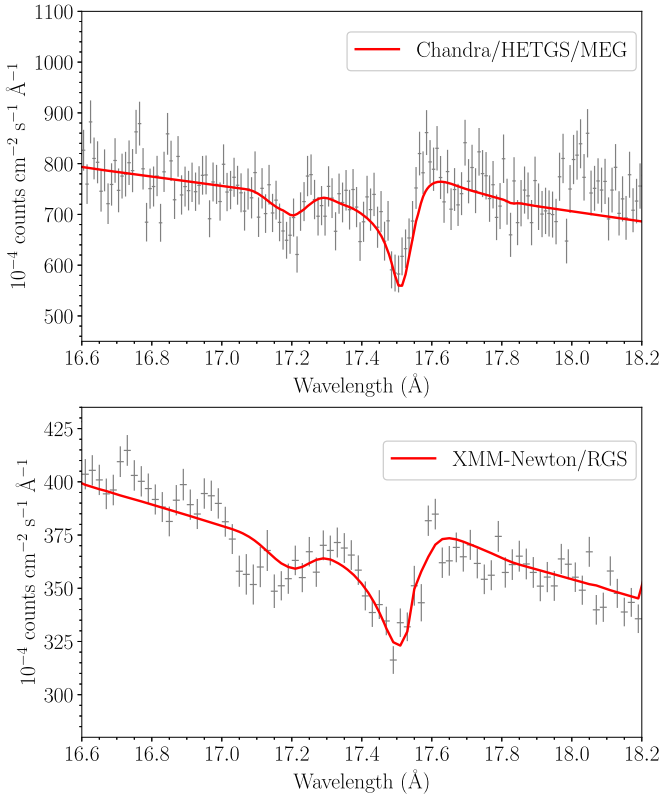

Figure 3. Best fit in the Fe L-edges toward Cygnus X-2. Top: Chandra/HETGS spectrum. Bottom: XMM-Newton/RGS spectrum.

In summary, our analysis confirms that the dust column density is consistent with earlier findings (Psaradaki et al. 2023), demonstrating the reliability of our method. We find a dust column density of $(7.9 \pm 1.6) \times 10^{16}$ cm^{-2}. Moreover, we have integrated the Fe II gas into our modeling, creating a consistent overall picture of how iron is distributed in the line of sight toward Cygnus X-2. We find that the majority of iron is in solids, while Fe II accounts for the atomic phase iron, about 4%.

5. Simultaneous Fit of the X-Ray and FUV Spectrum: O K-edge

Neutral gas-phase oxygen is highly abundant in the ISM. Large gas-phase column densities and the strong oscillator strength of the 1302 Å absorption line of O I found in the COS spectrum mean that this line is highly saturated. This typically puts the O I absorption line in the transition region between flat and damped on a curve of growth (Draine 2011). In the regime of the damped portion of the curve of growth, the core of the absorption line is totally saturated, but the "damping wings" of the line provide measurable partial transparency. This gives the possibility of measuring the abundance of neutral oxygen through the COS spectrum, and the only possibility for measuring its abundance comes from fitting the line profile, including the damping wings. Fortunately, gaseous O I also has prominent absorption features in the X-ray, near the K-shell photoelectric edge of oxygen, around 23 Å (0.55 keV). These features are typically optically thin and closer to the linear portion of the curve of growth (Juett et al. 2004). Therefore, we can more accurately constrain the gaseous abundance of O I and solid-phase components of interstellar oxygen through a simultaneous fit of the UV and X-ray data sets.

We limit our fit to the O I-bearing spectra from HST/COS and the X-ray portion of the O K-edge (19–25 Å) using XMM-Newton/RGS data. We use the `sectors` option in `SPEX` to fit the two data sets with a different continuum model, while the same ISM model is used in both sectors. For the FUV continuum, we use a phenomenological power-law component (`pow`), and for the X-ray continuum, we adopt the best-fit continuum parameters from Psaradaki et al. (2020). We let the X-ray continuum free, but we keep the FUV continuum frozen to the initial values found from a preliminary fit in `SPEX`. To model the O I features in the X-ray, we employ the `SPEX hot` model with the plasma temperature frozen to the minimum value of 10 K. The O I abundance is scaled from the model $N_{\rm H}$ column density, following protosolar oxygen values tabulated in Lodders (2003). $N_{\rm H}$ (and thereby the O I column density) is left as a free parameter. We add a Gaussian prior on $N_{\rm H}$ of 2×10^{21} cm^{-2}, consistent with the work of Kalberla et al. (2005), with a 10% dispersion. We freeze the depletion of Fe, Si, and Mg to 0.1, according to the values found in Rogantini et al. (2019), Zeegers et al. (2019), and Psaradaki et al. (2023). The depletion of oxygen is a free parameter, but we add a Gaussian prior of 0.95 with 10% dispersion to limit known degeneracies between this parameter and $N_{\rm H}$. Finally, we let the velocity-broadening parameter (b) and the velocity shift of the lines (z_v) be free in order to determine the kinematics of the O I line.

The O K-edge spectral region includes transitions of other ions, such as O II and O III, along with highly ionized O that is likely intrinsic to the X-ray binary (e.g., Juett et al. 2004; Pinto et al. 2010; Costantini et al. 2012; Gatuzz et al. 2016; Psaradaki et al. 2020). These ions are included in the fit via the `slab` model in `SPEX`. The ionic column densities of the O II, O III, and O IV lines are left as free parameters, while the highly ionized lines are frozen to the values found in Psaradaki et al. (2020). Oxygen absorption by dust is provided by the `amol` model in `SPEX`, which uses the dust extinction cross section computed from laboratory data described in Psaradaki et al. (2020). We used the best-fit compound from that work, amorphous pyroxene, (Mg, Fe)SiO_3, as the only dust species in the fit, leaving the column density free.

We combine our newly developed analysis pipelines, described in Sections 3 and 4, to fit the X-ray and FUV spectra simultaneously. The log-likelihood function used in this fitting procedure combines the chi-square statistic for the UV data with the Cash statistic obtained from the X-ray data. This method allows for a comprehensive and robust evaluation of the data from various spectral regions. To achieve convergence of the MCMC chain, we run the code for 200 iterations and 80 walkers for the 100 free parameters of the study. For the burn-in phase, we initiated the walkers in a normal distribution around the best-fit parameters found via `SPEX` and run MCMC for 50 steps. In Table 4, we summarize all the free parameters in this study and the best-fit values. We present the best fit in Figure 4 and the corresponding posterior distribution in Figure 5. The best fit suggests a slight overabundance of oxygen, 1.1 ± 0.1, compared to the Lodders & Palme (2009) abundance table.

6. Discussion

The HST/COS spectrum reveals at least two discrete absorbers with distinct velocity components. As shown in

Table 4
Best-fit Parameters for the Oxygen Spectral Region

Component	Parameter	Value
bb	T (keV)	0.18 ± 0.01
	$\log(\mathrm{norm_{bb}})$ (10^{16} m^{-2})	-5.07 ± 0.04
hot	N_{H} (10^{21} cm^{-2})	2.0 ± 0.1
	z_v (km s^{-1})	-40 ± 2
	b (km s^{-1})	17.0 ± 0.4
	$\mathrm{O_{abund}}$	1.1 ± 0.1
	log(O I) (cm^{-2})	18.04 ± 0.03
slab	log(O II) (cm^{-2})	<16.7
	log(O III) (cm^{-2})	<15.8
	log(O IV) (cm^{-2})	<16.4
amol	N_{dust}(10^{16} cm^{-2})	$8.13^{+0.92}_{-1.07}$

Note. The values are a result of the simultaneous fit of the FUV and X-ray spectral lines using SPEX models and emcee. N_{H} is the neutral hydrogen column density in the line of sight; z_v is the velocity shift of the absorber; $\log(\mathrm{norm_{bb}})$ is the logarithm of the blackbody normalization; N_{dust} is the total column density of dust; b refers to the line velocity broadening; O II, O III, and O IV correspond to the ionic column densities from the slab model; $\mathrm{O_{abund}}$ is the total O abundance scale factor relative to the abundance table of Lodders & Palme (2009); and O I is the implied column density of this ion from the hot model.

Figure 1, the interstellar absorption lines from the Fe II ion indicate two blueshifted components, one with velocity shift of -37 ± 4 km s^{-1} and one with -96 ± 5 km s^{-1}. Similarly, S II shows two components, one at -20 ± 2 km s^{-1} and one at -84 ± 2 km s^{-1} away from the rest-frame velocity. We used the kinematic distance calculator of Reid et al. (2014)[17] to estimate the distance to the Fe II and S II absorbers. Our analysis revealed that the components corresponding to Fe II are situated at distances of approximately 2.38 ± 0.35 and 5.01 ± 0.3 kpc, while for S II, we found distances of 1.44 ± 0.45 and 4.5 ± 0.3 kpc, respectively. The velocity shifts and cloud distances of the S II and Fe II components show some inconsistency within the margins of error. However, given their close proximity and the similarity in their ionization potentials, it is plausible that they arise from similar locations. If this is the case, then those two systems are likely ≈1–3 and 4–5.5 kpc away. For the singly ionized form of carbon C II, we were able to constrain a velocity shift of the first spectral component to -19 ± 2 km s^{-1}, likely associated with the nearer S II system. The second component is too weak to obtain a good fit when the line-of-sight velocity is left as a free parameter, so this value was frozen to -95 km s^{-1} in order to obtain a column density measurement.

Our discussion is organized into several parts. First, we review existing literature on standard abundance tables for the elements we are studying, and we use neon as a reference point for comparison. Next, we introduce a Cloudy grid that helps us compare our findings from both X-ray and FUV data regarding the column density ratios of different ions. Then, we present individual discussions for each element. Finally, we highlight discrepancies in the atomic data used for iron K-shell absorption in the literature.

[17] http://bessel.vlbi-astrometry.org/revised_kd_2014

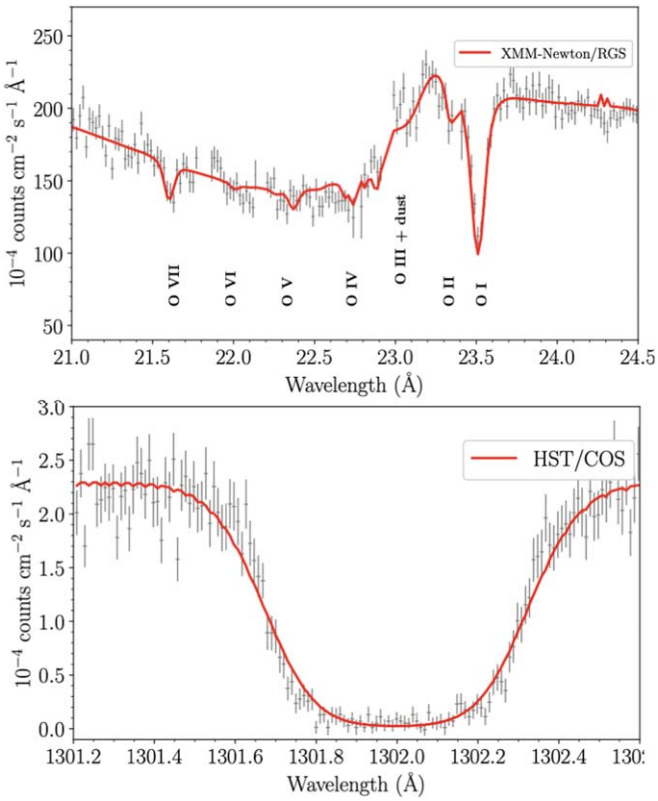

Figure 4. Best fit in the O K-edge and O I line profile in the HST/COS. Top: XMM-Newton/RGS. Bottom: HST/COS.

6.1. Elemental Abundances across the Literature and Cloudy

In Table 5, we report the abundance of O, Fe, C, S, and Ne among the different values found in the literature in standard units of $\log(\mathrm{X/H}) + 12$, where X/H represents the abundance of each element with respect to hydrogen. Anders & Grevesse (1989) present abundance tables for both meteoric and solar photosphere data. For our comparisons, we assume the photospheric values, although the two sets are generally consistent with each other, except for a few elements. For Fe, the solar value is 7.67 ± 0.03, while the meteoric is 7.51 ± 0.01. Similarly, the tabulated values from Grevesse & Sauval (1998), Lodders (2003), and Asplund et al. (2009, 2021) refer to the solar photospheric values. Wilms et al. (2000) present a model for the absorption of X-rays in the ISM. The selected values come from the adopted abundance of the ISM based on Cardelli et al. (1996), Snow & Witt (1996), and Meyer et al. (1998). Lastly, we also include in the comparison B-type star elemental abundances from Nieva & Przybilla (2012). In this study, our spectral models are based on the protosolar abundances as provided by Lodders & Palme (2009), which serve as the default abundance set in SPEX. In Figure 6, we present a comparative analysis of the elemental abundances listed in Table 5 for the elements under investigation in our study. Variations in the reported values make it important to note that the choice of the reference abundance table can have an impact on the resulting measured abundances.

Because it is a noble gas, neon will not deplete into dust grains. Thus, it can serve as a suitable reference for comparing the observed abundance of elements, providing an alternative to hydrogen, which does not provide any spectral features in

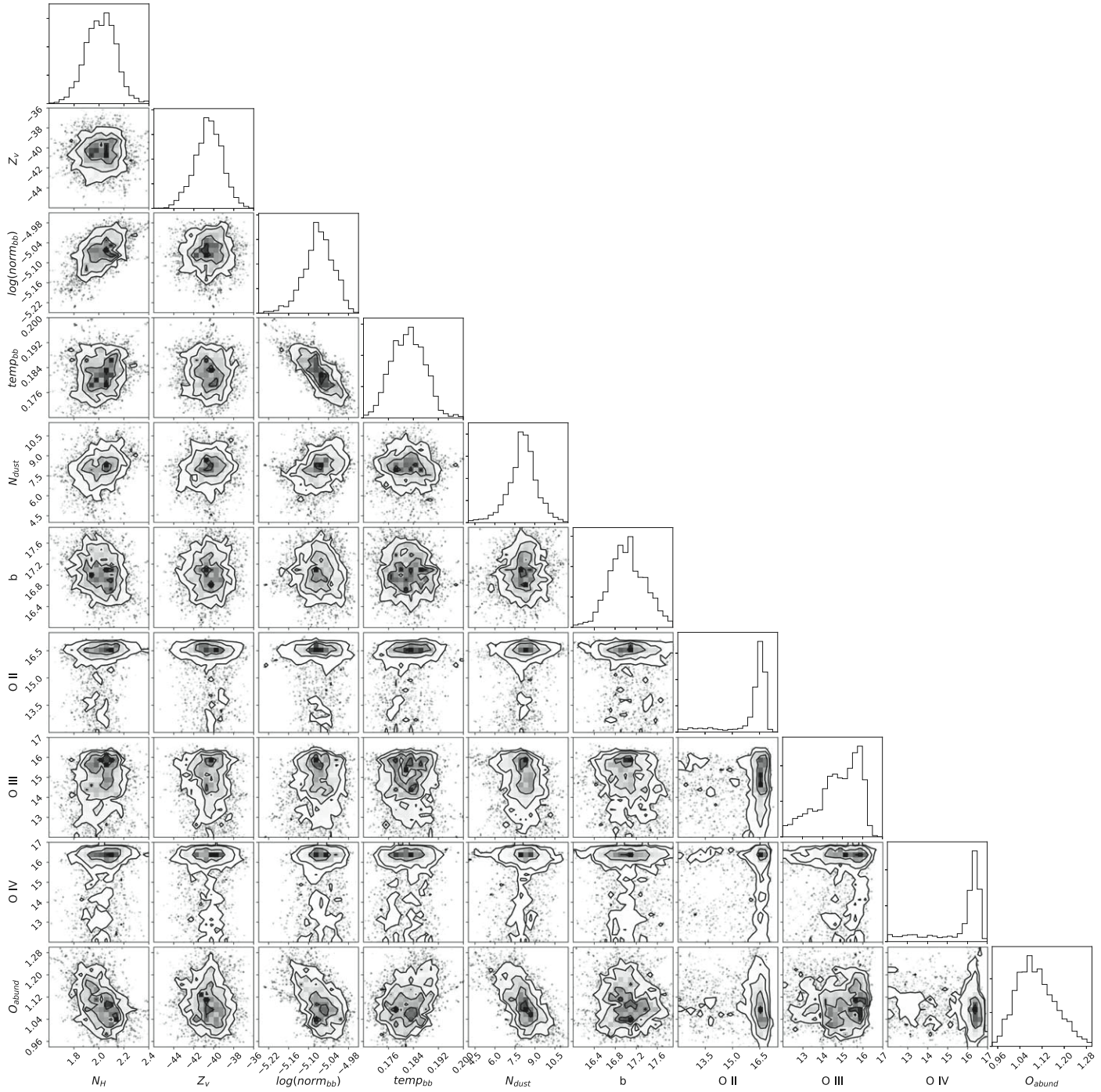

Figure 5. Posterior distribution for the simultaneous FUV and X-ray spectrum in the oxygen region. The distribution compares each pair of free parameters of the fit with two-dimensional histograms. The parameters in the plot correspond to the following quantities: $N_{\rm H}$ is the neutral hydrogen column density in units of 10^{21} cm^{-2} along the line of sight; z_v is the velocity shift in km s^{-1}; log(norm$_{\rm bb}$) is the logarithm of the blackbody normalization; $N_{\rm dust}$ is the total column density of dust in 10^{18} cm^{-2}; b refers to the line velocity broadening in km s^{-1}; O II, O III, and O IV correspond to the logarithmic ionic column densities in cm^{-2}; and O$_{\rm abund}$ is the O abundance scale factor relative to Lodders & Palme (2009).

the X-ray band. The last four columns of Table 5 display the calculated X/Ne ratio for each of the literature abundance tables. The Ne abundance is determined through the fit of the Ne K-edge in the X-ray spectrum from Psaradaki et al. (2023), and it represents the summed abundance of Ne I, Ne II, and Ne III, which is 2.1×10^{17} cm^{-2}. In the final row of Table 5, we present our computed value for log(X/Ne). In Figure 6, we visualize the results of Table 5, showing the deviations of the literature standard abundance tables for Fe, O, and S compared to neon, with the values of this work derived from FUV and X-ray observations. We will revisit this comparison of elemental abundances with neon in the following sections, where we will explore individual discussions of the elements under study.

We further use the spectral synthesis code `Cloudy` (version 2017; Ferland et al. 2017) and run a grid of models over a wide range of ionization parameters (ionizing photon density) and metallicity values for a neutral hydrogen column density of

Table 5
Literature Standard Abundances for the Elements in This Study

References	log(O/H) + 12	log(Fe/H) + 12	log(C/H) + 12	log(S/H) + 12	log(Ne/H) + 12	log(O/Ne)	log(Fe/Ne)	log(S/Ne)
Anders & Grevesse (1989)	8.93 ± 0.035	7.67 ± 0.03	8.56 ± 0.04	7.21 ± 0.06	8.09 ± 0.10	0.84 ± 0.10	-0.42 ± 0.10	-0.88 ± 0.01
Grevesse & Sauval (1998)	8.83 ± 0.06	7.5 ± 0.05	8.52 ± 0.06	7.33 ± 0.11	8.08 ± 0.06	0.75 ± 0.08	-0.58 ± 0.08	-0.75 ± 0.11
Wilms et al. (2000)[a]	8.69	7.43	8.38	7.09	7.94	0.75	−0.51	−0.85
Lodders (2003)	8.69 ± 0.05	7.47 ± 0.03	8.39 ± 0.04	7.19 ± 0.04	7.95 ± 0.10	0.74 ± 0.11	-0.48 ± 0.10	-0.76 ± 0.10
Lodders & Palme (2009)[b]	8.73 ± 0.07	7.45 ± 0.08	8.39 ± 0.04	7.14 ± 0.01	8.05 ± 0.10	0.68 ± 0.12	-0.6 ± 0.13	-0.91 ± 0.10
Asplund et al. (2009)[c]	8.69 ± 0.05	7.5 ± 0.04	8.43 ± 0.05	7.12 ± 0.03	7.93 ± 0.10	0.76 ± 0.11	-0.43 ± 0.1	-0.81 ± 0.10
Nieva & Przybilla (2012)[d]	8.76 ± 0.04	7.52 ± 0.03	8.33 ± 0.04	⋯	8.09 ± 0.05	0.67 ± 0.06	-0.57 ± 0.06	⋯
Asplund et al. (2021)	8.69 ± 0.04	7.46 ± 0.04	8.46 ± 0.04	7.12 ± 0.03	8.06 ± 0.05	0.63 ± 0.10	-0.60 ± 0.06	-0.94 ± 0.06
This study[e]						0.81 ± 0.03	-0.41 ± 0.11	$-1.35^{0.04}_{0.05}$

Notes. The standard abundances are expressed in logarithmic units, with hydrogen 12.0 by definition.
[a] Note that these values come from the adopted abundance of the ISM based on Cardelli et al. (1996), Snow & Witt (1996), and Meyer et al. (1998).
[b] Used in this study and default set of abundances in SPEX.
[c] We refer to the photospheric values.
[d] Abundances derived from B-type stars.
[e] The log(O/Ne) ratio is the sum of the predicted O I abundance that we obtain from a simultaneous X-ray and FUV fit and the solid-phase oxygen. For the log(Fe/Ne) ratio, we used the combined contribution of solid iron and atomic Fe II. The log(S/Ne) ratio comes from the S II value only resulting from the FUV fit. The Ne abundance is determined through the fit of the Ne K-edge in the X-ray spectrum from Psaradaki et al. (2023); in particular, it represents the summed abundance of Ne I, Ne II, and Ne III.

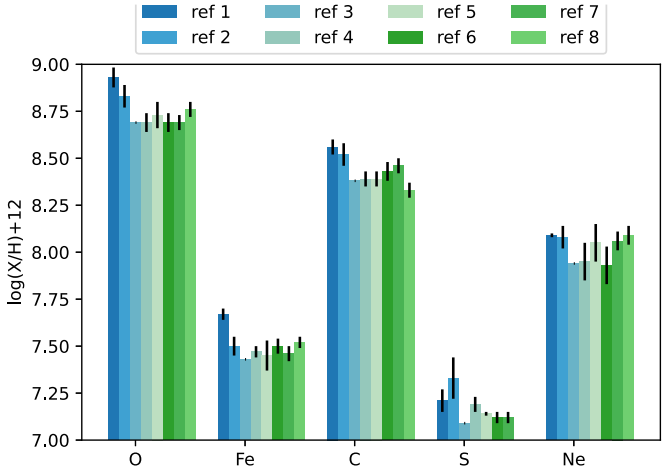

Figure 6. Comparison of the different abundance tables for every element, where ref 1: Anders & Grevesse (1989); ref 2: Grevesse & Sauval (1998); ref 3: Wilms et al. (2000); ref 4: Lodders (2003); ref 5: Lodders & Palme (2009); ref 6: Asplund et al. (2009); ref 7: Asplund et al. (2021); and ref 8: Nieva & Przybilla (2012).

2×10^{21} cm^{-2}. The ionization parameter U is defined as the ratio between the number densities of ionizing photons and hydrogen ($U \equiv n_\gamma / n_{\rm H}$), and we allow this parameter to vary from $\log U = -4$ to 0 by 0.25 dex. We also vary $\log Z/Z_\odot = -2$ to $+0.5$ in steps of 0.1 dex. We adopt a photoionizing spectrum from the Milky Way that includes a contribution from the extragalactic UV background (Fox et al. 2005) and assume thermal and ionization equilibrium for a plane-parallel slab geometry with a uniform density. We use the "grains ISM" command to specify grains with a size distribution and abundance consistent with those in the Milky Way and additionally employ the "metals deplete" command in our models to deplete elements that are included in grains, e.g., Fe, according to the work of Jenkins (2009). We utilize the `Cloudy` grids to compare between the ratios of the ions investigated in this study and the corresponding values predicted by `Cloudy`. We found that the relative abundances of each gas-phase ion were relatively insensitive to the magnitude of ionization parameter U for the photoionizing spectrum used in this run. We use $\log U = -5$ as our fiducial value in the discussion below.

First, we compare our observed ion abundances for oxygen with those predicted by `Cloudy` in scenarios where elements are not depleted into dust. This approach allows us to assess the predicted ion quantities in the case of excluding the influence of the dust phase, thereby discerning any disparities. Using `Cloudy`, we have determined that O II/O I $= 4.62 \times 10^{-4}$ and O III/O I $= 1.2 \times 10^{-7}$. Neutral oxygen gas is thereby expected to significantly dominate the neutral ISM abundance when compared to O II and O III, with O III being the least abundant among these ions. However, `Cloudy` functions as a photoionized model, diverging from the primarily collisionally ionized models used in the `hot` model of `SPEX`, and one should exercise caution when comparing to the absolute value of the ionic ratios. Through simultaneous fitting of both X-ray and UV data, we established upper limits for the ionic column densities of O II, O III, and O IV ions (Table 4). With the exception of O III, these upper limits are consistent with the derived values of Gatuzz et al. (2018) for the same source.

6.2. The Abundance and Depletion of Fe

Understanding the exact reservoirs of iron in the diffuse ISM is still an open question. Our X-ray fits yield a column density of solid-phase iron of 3.9×10^{16} cm^{-2}. The atomic component is in Fe II and contributes to the total column density through two distinct absorption systems (Table 3), amounting to 2×10^{15} cm^{-2}. Our `Cloudy` simulations, detailed in Section 6.1, indicate that the Fe I/Fe II ratio should be approximately 2.5×10^{-3}, while the Fe III/Fe II ratio is on the order of 10^{-6}. These findings suggest that Fe II is the dominant form of gas-phase iron in the neutral ISM, with Fe I and Fe III concentrations being negligible. The abundance of Fe II is still relatively small compared to the abundance of iron in solid form, accounting for merely 4% of the total iron content. The remaining 96% resides in solid-state structures in the form of amorphous pyroxene ($Mg_{0.75}Fe_{0.25}SiO_3$) and metallic iron. This dust grain mineralogy was previously found in Psaradaki et al. (2023), and it is assumed in this study. However, the dust column density of each compound is free, and it is found to be $<6.1 \times 10^{17}$ and $<1.2 \times 10^{16}$ cm^{-2} for the amorphous pyroxene and metallic iron, respectively. Additionally, we examined the scenario where Fe exists principally in its metallic form, as detailed in Westphal et al. (2019) for the observation of Cygnus X-1. However, when applying this model to the case study of Cygnus X-2, we observed a less optimal fit. The suggestion of metallic iron as a compound needs further investigation, primarily due to uncertainties in the energy calibration across various measurements of this compound in the literature (Psaradaki 2021; E. Costantini et al. 2024, in preparation; Corrales et al. 2024).

The selection of the MRN dust size distribution could potentially have an effect on the calculation of the dust column density. In particular, the phenomenon of self-shielding may play a role in diminishing the overall iron column available for photoelectric absorption (Wilms et al. 2000). In this case, strong absorption prevents X-rays from penetrating the inner portions of the dust grain, and a smaller fraction of the total metal column contributes to the absorption edge (Corrales et al. 2016). Our study incorporates self-shielding, and we have considered the extinction (scattering + absorption) cross section in our spectral modeling. However, this effect is anticipated to be particularly noticeable in regions of the ISM containing large grains, approaching the upper limit of the dust size distribution employed in our investigation. Consequently, it is plausible that some of the depleted iron is located within populations of large grains, specifically those exceeding 0.25 μm in size. Other size distributions beyond the MRN, such as those employed in Zubko et al. (2004) and Weingartner & Draine (2001), will be examined in a future study.

We extend our calculations to determine the combined abundance of iron in both gaseous and dust components, comparing it to established standard abundance values found in the literature. The third column in Table 5 presents a comparison of the iron abundance figures, denoted in units of log(Fe/H) + 12. Taking into account the associated uncertainties, our iron abundance estimation from our best fit is 7.38 ± 0.33, which takes into consideration iron in dust (comprising silicates and metallic iron) and Fe II. This result is in agreement with the standard abundance tables. Moreover, in Table 5 and Figure 7 (left panel), we show a comparison of the iron abundance tables compared to neon. Overall, there is consistent behavior between our calculated log(Fe/Ne) value,

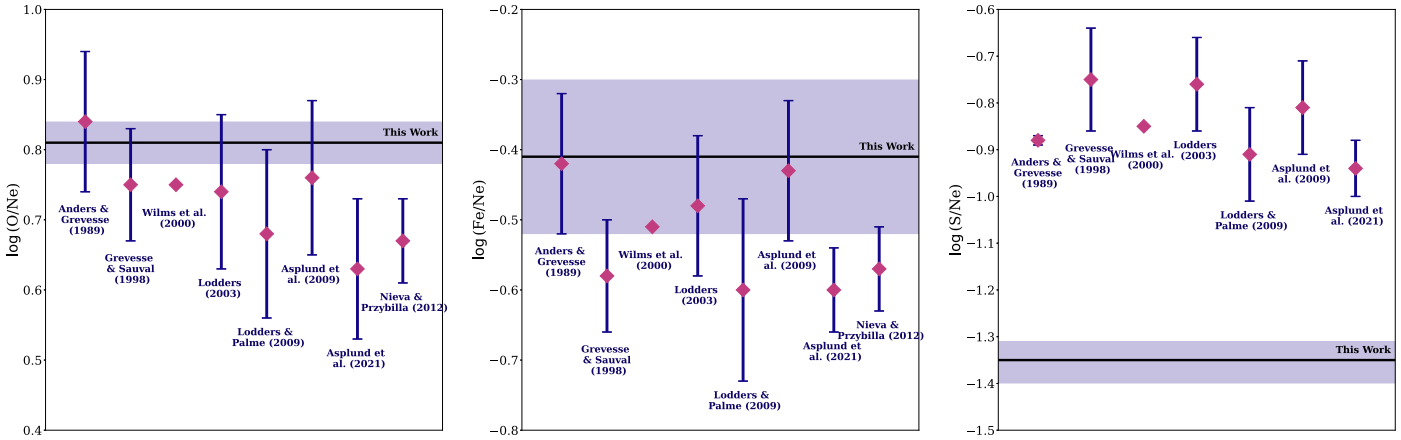

Figure 7. Comparison of the literature standard abundance tables of Fe, O, and S with the values of this work derived from FUV and X-ray observations presented in Table 5. The log(O/Ne) ratio is the sum of the predicted O I abundance that we obtain from a simultaneous X-ray and FUV fit and the solid-phase oxygen. For the log (Fe/Ne) ratio, we used the combined contribution of solid iron and atomic Fe II. Please note that the log(S/Ne) ratio comes from the S II value only resulting from the FUV fit. The Ne abundance is determined through the fit of the Ne K-edge in the X-ray spectrum from Psaradaki et al. (2023); in particular, it represents the summed abundance of Ne I, Ne II, and Ne III.

derived from spectral fitting of X-ray and UV data, and the standard abundance tables reported in the literature, with the exception of the most recent work of Asplund et al. (2021).

6.3. Where Is Sulfur?

In the COS spectrum of Cygnus X-2, we have identified singly ionized atomic sulfur lines (S II) at wavelengths of 1250.58 and 1253.81 Å. These spectral lines are associated with two distinct velocity clouds. The first cloud exhibits a column density of approximately $(7.4 \pm 0.5) \cdot 10^{15}\,\mathrm{cm}^{-2}$, and the second cloud shows a weaker transition with a column density of approximately $(1.9 \pm 0.1) \cdot 10^{15}\,\mathrm{cm}^{-2}$. When examining Table 5 and the right panel of Figure 7, we observe that the S II/Ne ratio derived from our analysis is underabundant compared to the total S/Ne ratio calculated from the literature. This suggests that there should be another reservoir of sulfur other than S II in the diffuse sight line of Cygnus X-2.

`Cloudy` modeling further predicts that the S I/S II ratio is 2.8×10^{-4}, implying that the remaining sulfur is not in the neutral gas phase. Similarly, the S II/S III ratio is 7.1×10^{-4}. These predictions imply that the remaining sulfur is not expected to be in the form of S I or S III; instead, it could be bound within molecules or dust particles. However, it is essential to exercise caution when utilizing the `Cloudy` ratios in this context. `Cloudy` operates as a photoionized model, presenting a contrast to the predominantly collisionally ionized models employed in the `hot` model of `SPEX` and widely adopted in previous studies. Moreover, in Gatuzz et al. (2024), the S K-edge has been examined using high-resolution Chandra/HETGS spectra of 36 low-mass X-ray binaries. In the case of Cygnus X-2, their ionic column density estimates appear to disagree with the `Cloudy` predictions. However, only upper limits of the ionic column densities were able to be provided.

Sulfur in dust species can take on various forms, including FeS or FeS_2, or even exist within GEMS (Bradley 1994), where the FeS particles would be more concentrated on the surface of the glassy silicate. However, studies have demonstrated that GEMS are less favored as a plausible component of interstellar dust (Keller & Messenger 2011, 2013; Westphal et al. 2019). In Psaradaki et al. (2023), we used newly computed dust extinction models of astrophysical dust analogs for the Fe L-edges including FeS or FeS_2. However, strong evidence for these species was not found in those works. It has been discussed in the literature that sulfur does not appear to change depletion in the diffuse ISM, suggesting that it does not easily get incorporated into dust (Sembach & Savage 1996). However, in molecular clouds, sulfur can be included in aggregates such as H_2S or SO_2 (Duley et al. 1980). Inclusion into simple atomic sulfur or sulfur ices has been proposed to solve the missing-sulfur problem in dense molecular clouds (Vidal et al. 2017). We examined the three-dimensional maps of interstellar dust reddening, which are based on Pan-STARRS 1 and Two Micron All Sky Survey photometry and Gaia parallaxes[18] (Green et al. 2019 and references therein). These maps trace the dust reddening as a function of both angular position on the sky and distance. Using these maps, we did not find any steep jump in the line-of-sight reddening. This could suggest that the line of sight toward Cygnus X-2 is rather diffuse and does not cross a dense molecular cloud. Thus, the nature of the missing sulfur in the Cygnus X-2 sight line, as determined in this study, is still a mystery.

A comprehensive understanding of sulfur depletion within dust particles can be achieved through the examination of the sulfur K-edge at 2.48 keV in X-ray spectra. Unfortunately, the column density toward Cygnus X-2 falls short in providing the necessary optical depth to study the photoabsorption edge of sulfur. Moreover, the current X-ray instruments utilized in this study lack sufficient energy resolution at this critical energy range. The recently launched X-ray Imaging and Spectroscopy Mission (XRISM) will enable us to directly study the photoabsorption edge of sulfur (e.g., Costantini et al. 2019) and determine the dust inclusion of this element.

6.4. The Carbon Abundance

The gas-phase carbon in the neutral ISM could be primarily in the form of singly ionized species, C II, because the C I ionization energy is lower than that of H I, and the C II ionization energy is above that of H I. Using `Cloudy`, we indeed find that the C I/C II ratio is 3.1×10^{-3}. Surprisingly,

[18] http://argonaut.skymaps.info/

we measure comparable column densities of C I and C II from the FUV spectral fit. We find that the total column density of the C II absorbers in the line of sight is $(4.7 \pm 0.3) \times 10^{14}\,\mathrm{cm}^{-2}$, while for C I, we find $3.6^{+1.1}_{-0.6} \times 10^{14}\,\mathrm{cm}^{-2}$.

We compare these values with carbon-related results available in the existing literature. Gatuzz et al. (2018) studied the C K-edge using high-resolution Chandra spectra of four novae during their super-soft-source state. They found column densities of C II in the range of $(1.8–3.5) \times 10^{17}\,\mathrm{cm}^{-2}$, which is inconsistent with our values in Table 3. Moreover, in the study by Sofia et al. (1997), the C II (2325 Å) equivalent width was measured in an absorption system directed toward the diffuse sight line of the τ Canis Majoris star. The results indicated a column density of $(7.57 \pm 2.52) \times 10^{16}\,\mathrm{cm}^{-2}$ for this system (and 10^6 C II/H I $= 135 \pm 46$). This finding was later complemented by Sofia & Parvathi (2009), who investigated various sight lines in the ISM with known hydrogen abundances utilizing HST/STIS data. Through the modeling of the strongest lines, they found C II column densities in the range $(1.97–6.19) \times 10^{17}\,\mathrm{cm}^{-2}$ across different lines of sight. In addition, Cardelli et al. (1993) detected C II in diffuse clouds toward ζ Oph using the Goddard High Resolution Spectrograph, reporting a column density of $1.8 \times 10^{17}\,\mathrm{cm}^{-2}$. Similarly, Cardelli et al. (1991) examined observations of ultraviolet interstellar absorption lines of dominant ion stages arising in the diffuse clouds in the direction of ξ Persei and focused on the same C II line, reporting a column density of $5 \times 10^{17}\,\mathrm{cm}^{-2}$. Collectively, these studies offer insights into the variations of C II column densities across different interstellar absorption systems. The column density of C II absorption observed in this study is significantly lower compared to the values reported above. One explanation could be that we are most likely probing C II that has been ionized by the ambient ISRF at the edges of the S II-bearing cloud, rather than a large photoionization region, as is expected around the massive O-type stars examined in the above works.

The C I in our study shows a different trend compared to the other ions studied here. The first and most dominant component shows a velocity shift of $-25\,\mathrm{km\,s}^{-1}$ between that of the nearer S II and Fe II absorbing region. Perhaps this stronger C I absorption could be arising from denser regions of the ISM that are shielded from the ISRF. The second, weaker component is redshifted compared to the rest-frame velocity. The source of this redshifted C I is unknown. Jenkins & Tripp (2011) studied the UV spectra of 89 stars using HST data. Based on the integrated C I absorption across all velocities, they determined that the column density of the C I absorbers falls within the range of approximately 2.4×10^{13}–$5.7 \times 10^{14}\,\mathrm{cm}^{-2}$ (lower limit). Our findings align with these results.

There are still uncertainties around the abundance and depletion of carbon within dust grains. Although carbon is a substantial element in grains, our understanding of the mechanisms through which dust grains incorporate carbon remains rather incomplete (Jenkins 2009). This topic continues to be an active area of study. Future advancements, including upcoming X-ray missions and innovative concepts like Arcus (Smith 2016), hold the potential to carry out in-depth spectroscopic analysis around the C K-edge, in particular the features of dust as well as C I (Costantini et al. 2019).

6.5. Discrepancies in the Available Fe X-Ray Atomic Data

In high-resolution X-ray spectroscopy, the choice of atomic data plays a crucial role in the analysis of the data and the interpretation of the results. In Psaradaki et al. (2020), we discussed the discrepancy between the atomic databases of SPEX and XSTAR for the oxygen ions from O I to O IV. We found out that the calibration of the energy scale of the different models can differ, and this can have an effect on the results, especially with future X-ray telescopes.

In this section, we examine the discrepancy in the atomic database for iron. We compare the atomic data implemented in SPEX with the available data of Fe I–Fe IV ions presented in the recent work of Schippers et al. (2021). The Fe I, Fe II, and Fe IV data in Schippers et al. (2021) have been taken from Richter et al. (2004), Schippers et al. (2017), and Beerwerth et al. (2019), respectively. In Figure 8, we compare the databases. From the plots, it is evident that there is a shift of about 2.7 eV between the SPEX atomic data and the models presented in Schippers et al. (2021), which is detectable with the energy resolution of the Chandra HETGS instrument.

We tested how the discrepancy between the atomic databases can affect the X-ray spectral fitting of Cygnus X-2. We shifted the absolute energy of the Fe I–Fe IV transitions in SPEX according to the energy calibration reported in Schippers et al. (2021). We kept the same model described in Section 4 and repeated the fit. Around the Fe L-edges, the X-ray absorption is dominated by the dust, while iron in atomic form is too weak to constrain the X-ray fits. We therefore achieved similar results. These discrepancies, however, will be more evident with future X-ray instruments, such as the spectral resolution capabilities demonstrated by the grating spectrometers of Arcus (Smith 2016).

7. Conclusions

In this work, we combined high-resolution X-ray and FUV spectroscopic data from Chandra, XMM-Newton, and HST. Our primary goal was to gain insights into the abundance and depletion patterns of oxygen, iron, sulfur, and carbon. To achieve this, we developed a novel analysis pipeline that involves a combined fitting of UV and X-ray data sets. This approach incorporates the consideration of the LSF of HST/COS for more accurate results. Our main conclusions can be summarized as follows.

1. HST's COS spectrum has unveiled intriguing insights into the line of sight toward Cygnus X-2. Our investigation of various ions, including Fe II, S II, and C II, has led to the identification of at least two distinct absorption systems, each exhibiting blueshifted velocity components. From the kinematics of the known Milky Way, these line-of-sight velocities correspond to ISM regions that are 1–3 and 4–5.5 kpc away. Neutral carbon presents an anomaly. The strongest absorption line has a blueshifted velocity consistent with the nearer absorption system. However, we also observe a redshifted velocity component, the source of which is unknown.
2. Cloudy simulations suggest that the majority of gaseous-phase interstellar iron should predominantly exist in the form of Fe II, with $\lesssim 10^{-3}$ of the gas-phase iron contributions coming from Fe I and Fe III. Moreover, we find that our derived iron abundance, accounting for the iron present in Fe II and dust, which comprises silicates and metallic iron, is consistent with the solar values from the literature listed in Table 5.
3. Cloudy simulations suggest that S II is expected to be the dominant gas-phase ion of sulfur, rather than S I or S III. However, the abundance of S II directly measured

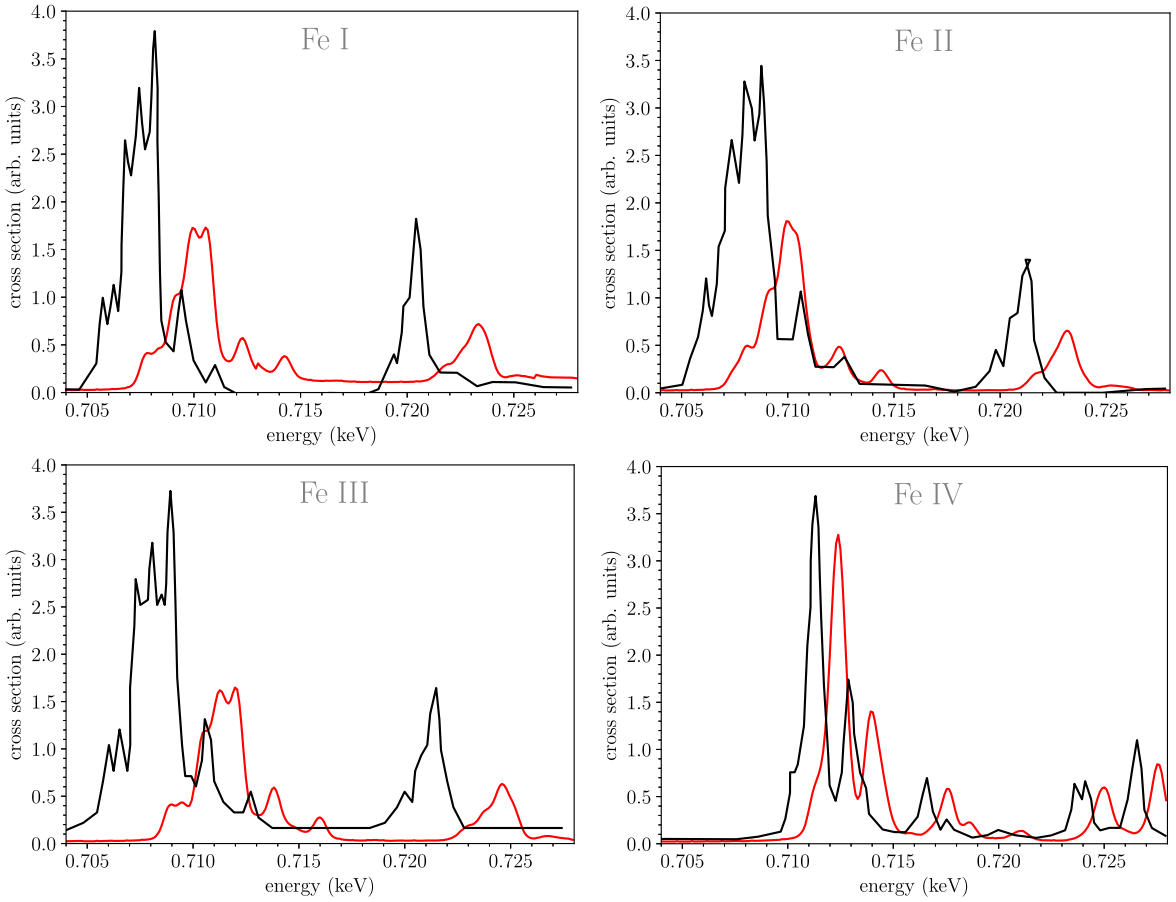

Figure 8. Comparison between the X-ray atomic database of SPEX (red) and Schippers et al. (2021; black) for Fe I, Fe II, Fe III, and Fe IV. The Fe I, Fe II, and Fe IV data in Schippers et al. (2021) have been taken from Richter et al. (2004), Schippers et al. (2017), and Beerwerth et al. (2019), respectively.

from the HST/COS data is much lower than expected from standard abundance arguments. It is apparent that an additional repository for sulfur is needed, possibly in the form of dust. Intriguingly, most X-ray analyses do not find strong signatures of FeS compounds (Westphal et al. 2019; Psaradaki et al. 2023; Corrales et al., submitted), prompting the exploration of alternative compounds. XRISM (launched 2023 September; Tashiro et al. 2020) has the collecting area and energy resolution to potentially resolve this issue. In particular, investigating the sulfur and iron K-edges simultaneously could unlock this mystery.

4. The X-ray atomic databases employed in high-resolution X-ray spectroscopy, particularly in the vicinity of the Fe L-edges, may be a source of additional uncertainty. Notably, deviations in energy scale have been observed, with discrepancies of up to 2.7 eV. These disparities will become even more pronounced in the context of future X-ray instruments with enhanced spectral resolution within the soft X-ray range, such as the Arcus concept mission (Smith 2016).

In conclusion, our investigation of the depletion and abundances of Fe, O, S, and C demonstrates the potential of combining X-ray and FUV data. This is a powerful way to determine the abundance of these elements in atomic form and then estimate their presence in dust species through high-resolution X-ray spectra. It is therefore encouraged to extend this study to more sight lines along the Galactic plane.

Acknowledgments

We thank the referee for the suggestions that helped to improve this paper. The authors would like to thank J. de Plaa for help with SPEX. This research has been supported by NASA's Astrophysics Data Analysis Program, grant No. 80NSSC20K0883, under the ROSES program NNH18ZDA001N. Support for this work was also provided by NASA through the Smithsonian Astrophysical Observatory (SAO) contract SV3-73016 to MIT for support of the Chandra X-Ray Center (CXC) and science instruments. CXC is operated by SAO for and on behalf of NASA under contract NAS8-03060.

Some of the data presented in this article were obtained from the Mikulski Archive for Space Telescopes (MAST) at the Space Telescope Science Institute. The specific observations analyzed can be accessed via doi:10.17909/vdjz-xn16. This paper also employs a list of Chandra data sets, obtained by the Chandra X-ray Observatory, contained in doi:10.25574/cdc.202.

ORCID iDs

I. Psaradaki https://orcid.org/0000-0002-1049-3182

References

Altobeli, N., Postberg, F., Fiege, K., et al. 2016, Sci, 352, 312
Anders, E., & Grevesse, N. 1989, Geochim. Cosmochim. Acta, 53, 197
Asplund, M., Amarsi, A. M., & Grevesse, N. 2021, A&A, 653, A141
Asplund, M., Grevesse, N., & Sauval, A. J. 2009, ARA&A, 47, 481
Beerwerth, R., Buhr, T., Perry-Sassmannshausen, A., et al. 2019, ApJ, 887, 189

Bradley, J. P. 1994, Sci, 265, 925
Brinkman, A., Gunsing, C., Kaastra, J., et al. 2000, ApJL, 530, L111
Canizares, C., Davis, J., Dewey, D., et al. 2005, PASP, 117, 1144
Cardelli, J. A., Mathis, J. S., Ebbets, D. C., & Savage, B. D. 1993, ApJL, 402, L17
Cardelli, J. A., Meyer, D. M., Jura, M., & Savage, B. D. 1996, ApJ, 467, 334
Cardelli, J. A., Savage, B. D., Bruhweiler, F. C., et al. 1991, ApJL, 377, L57
Cash, W. 1979, ApJ, 228, 939
Corrales, L., Valencic, L., Costantini, E., et al. 2019, BAAS, 51, 264
Corrales, L. R., García, J., Wilms, J., & Baganoff, F. 2016, MNRAS, 458, 1345
Corrales, L., Gotthelf, E. V., Gatuzz, E., et al. 2024, arXiv:2402.06726
Costantini, E., & Corrales, L. 2022, Handbook of X-ray and Gamma-ray Astrophysics (Berlin: Springer), 40
Costantini, E., Pinto, C., Kaastra, J. S., et al. 2012, A&A, 539, A32
Costantini, E., Zeegers, S. T., Rogantini, D., et al. 2019, A&A, 629, A78
Cowley, A. P., Crampton, D., & Hutchings, J. B. 1979, ApJ, 231, 539
de Plaa, J., Kaastra, J. S., Tamura, T., et al. 2004, A&A, 423, 49
de Vries, C. P., & Costantini, E. 2009, A&A, 497, 393
den Herder, J. W., Brinkman, A. C., Kahn, S. M., et al. 2001, A&A, 365, L7
Draine, B. T. 1989, in Proc. of IAU Symp. 135, Interstellar Dust, ed. L. J. Interstellar Dust & A. G. G. M. Allamandola (Dordrecht: Kluwer), 313
Draine, B. T. 2003, ARA&A, 41, 241
Draine, B. T. 2011, Physics of the Interstellar and Intergalactic Medium (Princeton. NJ: Princeton Univ. Press)
Draine, B. T., & Hensley, B. S. 2021, ApJ, 909, 94
Duley, W. W., Jones, A. P., & Williams, D. A. 1989, MNRAS, 236, 709
Duley, W. W., Millar, T. J., & Williams, D. A. 1980, MNRAS, 192, 945
Dwek, E. 1997, ApJ, 484, 779
Dwek, E. 2016, ApJ, 825, 136
Eckersall, A. J., Vaughan, S., & Wynn, G. A. 2017, MNRAS, 471, 1468
Ferland, G. J., Chatzikos, M., Guzmán, F., et al. 2017, RMxAA, 53, 385
Foreman-Mackey, D., Hogg, D. W., Lang, D., & Goodman, J. 2013, PASP, 125, 306
Fox, A. J., Wakker, B. P., Savage, B. D., et al. 2005, ApJ, 630, 332
Fruscione, A., McDowell, J. C., Allen, G. E., et al. 2006, Proc. SPIE, 6270, 586
García, J., Ramírez, J. M., Kallman, T. R., et al. 2011, ApJL, 731, L15
Gatuzz, E., García, J., Mendoza, C., et al. 2014, ApJ, 790, 131
Gatuzz, E., García, J. A., Kallman, T. R., & Mendoza, C. 2016, A&A, 588, A111
Gatuzz, E., Gorczyca, T. W., Hasoglu, M. F., et al. 2024, MNRAS, 527, 1648
Gatuzz, E., Ness, J. U., Gorczyca, T. W., et al. 2018, MNRAS, 479, 2457
Green, G. M., Schlafly, E., Zucker, C., Speagle, J. S., & Finkbeiner, D. 2019, ApJ, 887, 93
Grevesse, N., & Sauval, A. J. 1998, SSRv, 85, 161
Hony, S., Bouwman, J., Keller, L. P., & Waters, L. B. F. M. 2002, A&A, 393, L103
Huenemoerder, D. P., Mitschang, A., Dewey, D., et al. 2011, AJ, 141, 129
Ishii, H. A., Bradley, J. P., Bechtel, H. A., et al. 2018, PNAS, 115, 6608
Jenkins, E. B. 2009, ApJ, 700, 1299
Jenkins, E. B., Savage, B. D., & Spitzer, L. J. 1986, ApJ, 301, 355
Jenkins, E. B., & Tripp, T. M. 2011, ApJ, 734, 65
Jensen, A. G., & Snow, T. P. 2007, ApJ, 669, 378
Joachimi, K., Gatuzz, E., García, J. A., & Kallman, T. R. 2016, MNRAS, 461, 352
Jones, A. P., Köhler, M., Ysard, N., Bocchio, M., & Verstraete, L. 2017, A&A, 602, A46
Juett, A. M., Schulz, N. S., & Chakrabarty, D. 2004, ApJ, 612, 308
Kaastra, J. S. 2017, A&A, 605, A51
Kaastra, J. S., Raassen, A. J. J., de Plaa, J., & Gu, L. 2018, SPEX X-ray spectral fitting package, v3.05.00, Zenodo, doi:10.5281/zenodo.2419563
Kalberla, P. M. W., Burton, W. B., Hartmann, D., et al. 2005, A&A, 440, 775
Keller, L. P., & Messenger, S. 2011, GeCoA, 75, 5336
Keller, L. P., & Messenger, S. 2013, GeCoA, 107, 341
Kemper, F., de Koter, A., Waters, L. B. F. M., Bouwman, J., & Tielens, A. G. G. M. 2002, A&A, 384, 585
Kim, S.-H., & Martin, P. G. 1996, ApJ, 462, 296
Konstantopoulou, C., De Cia, A., Ledoux, C., et al. 2024, A&A, 681, A64
Lee, J. C., & Ravel, B. 2005, ApJ, 622, 970
Lodders, K. 2003, ApJ, 591, 1220
Lodders, K., & Palme, H. 2009, M&PSA, 72, 5154
Mathis, J. S. 1998, ApJ, 497, 824
Mathis, J. S., Rumpl, W., & Nordsieck, K. H. 1977, ApJ, 217, 425
McClintock, J. E., Remillard, R. A., Petro, L. D., Hammerschlag-Hensberge, G., & Proffitt, C. R. 1984, ApJ, 283, 794
Meyer, D. M., Jura, M., & Cardelli, J. A. 1998, ApJ, 493, 222
Miller, A., Lauroesch, J. T., Sofia, U. J., Cartledge, S. I. B., & Meyer, D. M. 2007, ApJ, 659, 441
Min, M., Waters, L. B. F. M., de Koter, A., et al. 2007, A&A, 462, 667
Morton, D. C. 1991, ApJS, 77, 119
Newville, M. 2014, RvMG, 78, 33
Nieva, M. F., & Przybilla, N. 2012, A&A, 539, A143
Pearson, K. 1900, Philosophical Magazine and Journal of Science, 50, 157
Pinto, C., Kaastra, J. S., Costantini, E., & Verbunt, F. 2010, A&A, 521, A79
Pinto, C., Kaastra, J. S., Costantini, E., & de Vries, C. 2013, A&A, 551, A25
Pinto, C., Kriss, G. A., Kaastra, J. S., et al. 2012, A&A, 541, A147
Poteet, C. A., Whittet, D. C. B., & Draine, B. T. 2015, ApJ, 801, 110
Psaradaki, I. 2021, PhD thesis, Anton Pannekoek Institute for Astronomy
Psaradaki, I., Costantini, E., Mehdipour, M., et al. 2020, arXiv:2009.06244
Psaradaki, I., Costantini, E., Rogantini, D., et al. 2023, A&A, 670, A30
Reid, M. J., Menten, K. M., Brunthaler, A., et al. 2014, ApJ, 783, 130
Richter, T., Godehusen, K., Martins, M., Wolff, T., & Zimmermann, P. 2004, PhRvL, 93, 023002
Rogantini, D., Costantini, E., Zeegers, S. T., et al. 2018, A&A, 609, A22
Rogantini, D., Costantini, E., Zeegers, S. T., et al. 2019, A&A, 630, A143
Savage, B. D., & Bohlin, R. C. 1979, ApJ, 229, 136
Savage, B. D., & Sembach, K. R. 1996, ARA&A, 34, 279
Schippers, S., Beerwerth, R., Bari, S., et al. 2021, ApJ, 908, 52
Schippers, S., Martins, M., Beerwerth, R., et al. 2017, ApJ, 849, 5
Schulz, N. S., Corrales, L., & Canizares, C. R. 2016, ApJ, 827, 49
Sembach, K. R., & Savage, B. D. 1996, ApJ, 457, 211
Smale, A. P. 1998, ApJL, 498, L141
Smith, R. K. e. a. 2016, Proc. SPIE, 9905, 99054M
Snow, T. P., Rachford, B. L., & Figoski, L. 2002, ApJ, 573, 662
Snow, T. P., & Witt, A. N. 1996, ApJL, 468, L65
Hirschauer, A. S. 2023, Cosmic Origins Spectrograph Instrument Handbook (Baltimore, MD: STScI), 15
Sofia, U. J., Cardelli, J. A., Guerin, K. P., & Meyer, D. M. 1997, ApJL, 482, L105
Sofia, U. J., & Parvathi, V. S. 2009, in ASP Conf. Ser. 414, Cosmic Dust—Near and Far, ed. T. Henning, E. Grün, & J. Steinacker (San Francisco, CA: ASP), 236
Steenbrugge, K. C., Kaastra, J. S., Crenshaw, D. M., et al. 2005, A&A, 434, 569
Takei, Y., Fujimoto, R., Mitsuda, K., & Onaka, T. 2002, ApJ, 581, 307
Tashiro, M., Maejima, H., Toda, K., et al. 2020, Proc. SPIE, 11444, 1144422
Tielens, A. G. G. M. 2001, in ASP Conf. Ser. 231, Tetons 4: Galactic Structure, Stars and the Interstellar Medium, ed. C. E. Woodward, M. D. Bicay, & J. M. Shull (San Francisco, CA: ASP), 92
Tielens, A. G. G. M., Seab, C. G., Hollenbach, D. J., & McKee, C. F. 1987, ApJL, 319, L109
Ueda, Y., Mitsuda, K., Murakami, H., & Matsushita, K. 2005, ApJ, 620, 274
van de Hulst, H. C. 1957, Light Scattering by Small Particles (New York: Wiley)
Vidal, T. H. G., Loison, J.-C., Jaziri, A. Y., et al. 2017, MNRAS, 469, 435
Weingartner, J. C., & Draine, B. T. 2001, ApJ, 548, 296
Westphal, A. J., Butterworth, A. L., Tomsick, J. A., & Gainsforth, Z. 2019, ApJ, 872, 66
Westphal, A. J., Stroud, R. M., Bechtel, H. A., et al. 2014, Sci, 345, 786
Whittet, D. C. B. 2003, Dust in the Galactic Environment (Bristol: IOP Publishing)
Whittet, D. C. B. 2010, ApJ, 710, 1009
Wilms, J., Allen, A., & McCray, R. 2000, ApJ, 542, 914
Wooden, D. H. 2008, SSRv, 138, 75
Yang, J., Schulz, N. S., Rogantini, D., et al. 2022, AJ, 164, 182
Yao, Y., Schulz, N. S., Gu, M. F., Nowak, M. A., & Canizares, C. R. 2009, ApJ, 696, 1418
Zeegers, S. T., Costantini, E., de Vries, C. P., et al. 2017, A&A, 599, A117
Zeegers, S. T., Costantini, E., Rogantini, D., et al. 2019, A&A, 627, A16
Zhukovska, S., Henning, T., & Dobbs, C. 2018, ApJ, 857, 94
Zubko, V., Dwek, E., & Arendt, R. G. 2004, ApJS, 152, 211